Reflection properties of the core-mantle boundary from global stacks of *PcP* and *ScP*

Steven E. Persh and John E. Vidale[1]

Department of Earth and Space Sciences, University of California, Los Angeles, California, USA

Received 29 August 2003; revised 4 February 2004; accepted 23 February 2004; published 22 April 2004.

[1] Seismic phases that reflect off the core-mantle boundary (CMB) are sensitive to the velocity and density contrasts between the base of the mantle and the core. We measure the amplitudes of CMB reflections to seek effects of large velocity reductions and possible density increases in proposed thin basal layers (ultralow-velocity zones, or ULVZs). We construct globally averaged envelope stacks of *PcP* and *ScP* in 3°-wide epicentral distance bins, correcting for propagation and source effects. We measure the amplitude ratios *PcP*/*P* and *ScP*/*P* and compare them with the predicted range dependence for preliminary reference Earth model (PREM) and several proposed ULVZ models. The amplitude ratios are not compatible with ULVZs containing 30% *S* wave velocity reductions or with a 3-km-wide core-mantle transition zone. The *PcP* data cannot distinguish between PREM and models with 10% reductions in both *P* wave velocity (V_P) and *S* wave velocity (V_S) and up to a 20% increase in density. The *ScP* data also match PREM closely but contain greater uncertainty from the correction for mantle attenuation. In well-sampled regions, lateral variations of reflection amplitudes mapped to bounce point locations are consistent with previous detections and nondetections of ULVZs. These results suggest that extreme velocity reductions near the CMB are not global features and that regions with large velocity reductions do not result from global phenomena such as phase changes in an isochemical mantle but rather from local thermal or compositional anomalies. *INDEX TERMS:* 7203 Seismology: Body wave propagation; 7207 Seismology: Core and mantle; 8124 Tectonophysics: Earth's interior—composition and state (1212); *KEYWORDS:* core-mantle boundary, ultralow-velocity zones, *PcP*, *ScP*

Citation: Persh, S. E., and J. E. Vidale (2004), Reflection properties of the core-mantle boundary from global stacks of *PcP* and *ScP*, *J. Geophys. Res.*, *109*, B04309, doi:10.1029/2003JB002768.

1. Introduction

[2] The discovery of thin layers with large low-velocity anomalies above the core-mantle boundary (CMB) has reshaped our ideas about the geodynamics and material properties in that region of Earth. Ultralow-velocity zones (ULVZs) are thin layers at the base of the mantle with large velocity reductions relative to average material at those depths. ULVZs have been modeled with thicknesses ranging from 5 to 50 km, *P* wave velocity (V_P) reductions of 10–20%, and *S* wave velocity (V_S) reductions of 10–50% [*Garnero and Jeanloz*, 2000], although trade-offs exist between the thickness and velocity reduction [*Garnero and Helmberger*, 1998] and there is only limited evidence for the V_S reduction. Density increases in ULVZs have also been suggested, but they are poorly constrained [*Garnero and Helmberger*, 1998]. Seismic arrivals used to identify ULVZs include delayed core phases ($SP_{diff}KS$ [*Garnero and Helmberger*, 1996]), scattered core phases (*PKP* [*Vidale and Hedlin*, 1998; *Wen and Helmberger*, 1998]), and precursors to core-reflected phases (*PcP* [*Mori and Helmberger*, 1995; *Revenaugh and Meyer*, 1997] and *ScP* [*Garnero and Vidale*, 1999; *Rost and Revenaugh*, 2003]). Possible explanations for ULVZs include partial melting [*Williams and Garnero*, 1996; *Holland and Ahrens*, 1997], phase transitions [*Garnero et al.*, 1998; *Sidorin et al.*, 1999], layering associated with subducted lithosphere or primordial differentiation [*Tackley*, 1998], reactions with core material [*Manga and Jeanloz*, 1996], partitioning of iron from mantle melt [*Knittle*, 1998], and a thin layer of finite rigidity at the top of the outer core [*Buffett et al.*, 2000; *Garnero and Jeanloz*, 2000].

[3] With about half the CMB sampled (44%), ULVZs cover ~12% of the surface [*Williams et al.*, 1998]. The zones vary laterally in their thicknesses and velocity contrasts [*Garnero et al.*, 1998], which may account for the lack of observation in some regions. ULVZ locations correlate with surface hot spots [*Williams et al.*, 1998], and ULVZs have been located under regions of presumed mantle upwelling [*Wen*, 2000; *Helmberger et al.*, 2000]. However, our knowledge of the global extent of ULVZs and lateral variation of their velocity and density structure

[1] Also at the Institute of Geophysics and Planetary Physics, University of California, Los Angeles, California, USA.

0148-0227/04/2003JB002768$09.00

remains incomplete. Models of ULVZ formation and their role in deep Earth dynamics depend on the resolution of these issues [*Garnero et al.*, 1998].

[4] CMB-reflected seismic phases such as *PcP* and *ScP* are especially useful for understanding ULVZs because of their extensive yet localized sampling of the CMB. In particular, their amplitudes are sensitive to the velocity and density contrasts at the boundary itself. ULVZs with extreme velocity reductions, a high degree of heterogeneity, or partial melt will affect amplitudes of CMB-reflected phases by changes in the impedance contrast, reduced sharpness of the boundary, or losses due to attenuation and scattering.

[5] Short-period regional seismic network seismograms have been stacked to search for precursor arrivals to core reflections that could result from ULVZ upper boundary reflections or reverberations within ULVZs [e.g., *Mori and Helmberger*, 1995; *Revenaugh and Meyer*, 1997; *Garnero and Vidale*, 1999; *Reasoner and Revenaugh*, 1999; *Persh et al.*, 2001], but global measurements of core reflectivity have not been performed since the global broadband network expanded dramatically. An examination of these phases with a global data set enables a consistent approach to measuring average global CMB reflectivity as well as lateral variations. Here we present results from a global study of CMB reflectivity with the short-period seismic phases *PcP* and *ScP*. We characterize the CMB by computing the amplitude ratios *PcP*/*P* and *ScP*/*P*. We measure globally averaged CMB reflection amplitudes and compare them with predictions for basal layering. We also compute reflection amplitudes from stacks that are binned by CMB bounce point location to explore lateral variations of CMB reflection properties.

2. Data and Processing

2.1. Data Selection

[6] We use data from the Fast Archive Recovery Method database of Global Seismographic Network waveforms maintained by the Incorporated Research Institutions for Seismology Data Management Center. The database consists of over 535,000 waveforms from over 3000 earthquakes occurring between 1988 and 2000. The waveforms were decimated to five samples per second.

[7] We identify events with source depths between 0 and 100 km and with moment magnitudes (M_W) between 6.0 and 7.0. The lower-magnitude bound serves to reject traces of insufficient signal-to-noise ratio; the upper bound is chosen so that the earthquake time functions are relatively brief. The seismograms are taken at teleseismic distances (30°–76° for *PcP* and 30°–65° for *ScP*). The lower distance limit avoids *P* arrivals complicated from upper mantle triplications, and the upper limit for *PcP* recognizes that the travel time difference from *P* is often less than the expected source duration at large epicentral distances. *ScP* has reached its reflection critical angle by 65°. We only use vertical components since CMB reflections are nearly vertically incident at the surface.

[8] We also apply signal-to-noise criteria. We measure the amplitude of *PcP* or *ScP* on the velocity seismograms and require a minimum ratio to the preevent noise level. To counter the bias toward selecting for large *PcP* or ScP, we impose an additional requirement that each seismogram meets a more stringent minimum *P*-to-noise ratio as well. For *PcP* the procedure yields between 5558 and 5756 seismograms, depending on the band pass, out of ~21,000 seismograms matching the source property criteria. For *ScP* the procedure yields between 3765 and 3972 seismograms, depending on the band pass, out of ~15,000 seismograms matching the source property criteria.

[9] The extent of global coverage is shown in Figure 1. The configuration of sources and stations is uneven over the globe. About 30% of the CMB surface is sampled by *PcP*, and ~25% is sampled by *ScP*, counting 15° × 15° grid elements with at least 10 hits. Nevertheless, this represents the best global sampling of the CMB so far achieved with core-reflected phases.

2.2. Computation of Envelope Stacks

[10] To compute stacks of seismograms from many different earthquakes, which will not sum constructively, we employ envelope stacking, in which the envelope functions of the seismograms are summed. The selected seismograms are demeaned, band-pass filtered (0.25–0.5 Hz, 0.5–1.0 Hz, and 1.0–2.0 Hz), and grouped in 3°-wide epicentral distance bins. We deconvolve the instrument response, compute the envelope function of each seismogram, and align at the predicted *PcP* or *ScP* arrival time using the International Association of Seismology and the Physics of the Earth 1991 seismological tables (iasp91) [*Kennett and Engdahl*, 1991]. To remove any baseline offset, we subtract the average background noise measured in a time window from 10 to 60 s before the *P* arrival. Because noise and signal sum in a root-mean-square sense, we square the envelope function in order to subtract noise properly [e.g., *Earle and Shearer*, 2001].

[11] We next apply amplitude corrections to account for source and path effects. The observed amplitude of *PcP* (A_{PcP}^{obs}) is the product of the amplitude leaving the source as compressional waves (A_P) with several factors: the radiation pattern (Φ), geometrical spreading (G), attenuation (Q), the instrument response (I), and the reflection coefficient (R_{PcP}) at the CMB,

$$A_{PcP}^{obs} = A_P \Phi G Q I R_{PcP}. \quad (1)$$

We can write similar expressions for A_P^{obs} and A_{ScP}^{obs}. The processing of each seismogram corrects for the factors Φ, G, Q, and I. In addition, we correct *ScP* to account for the greater amplitude in shear waves at the source. Then the amplitude ratio *PcP*/*P* or *ScP*/*P* will yield the reflection coefficient at the CMB.

[12] We use each event's Harvard centroid moment tensor catalog solution to calculate a correction factor for radiation pattern [*Aki and Richards*, 1980] with a water level of 0.2 to prevent artifacts from dividing by small values. We compute a multiplicative correction for geometrical spreading [*Lay and Wallace*, 1995].

[13] Attenuation is calculated at the frequency of the peak of the spectrum in each band pass, as measured from frequency domain stacks of a subset of the data. The peaks occur at about 0.3 Hz (0.25- to 0.5-Hz band pass), 0.55 Hz (0.5- to 1.0-Hz band pass), and 1.0 Hz (1.0- to 2.0-Hz band pass). There can be a trade-off between attenuation in the deep mantle and reflection coefficient at the CMB. Greater

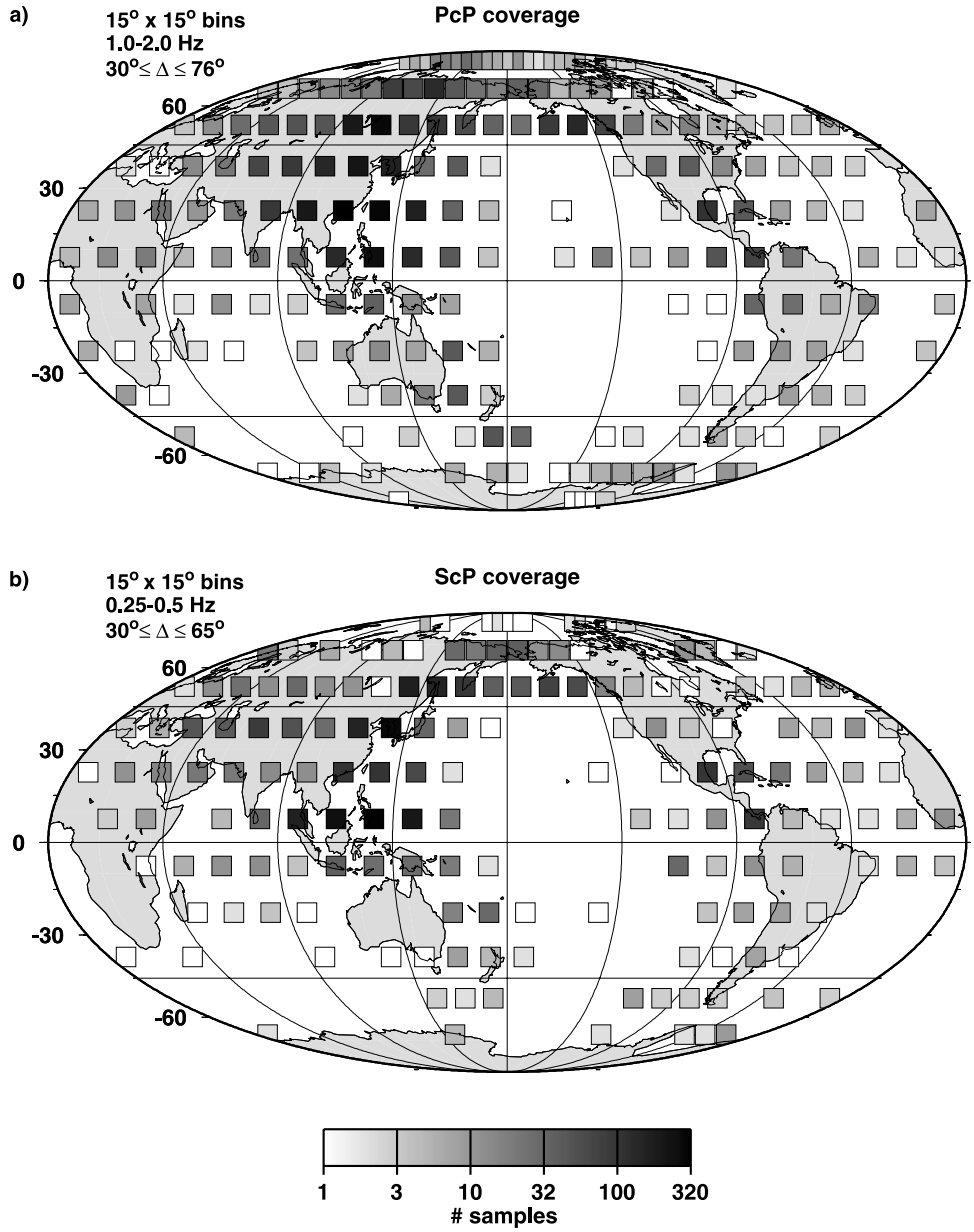

Figure 1. (a) Number of *PcP* bounce points in 15° × 15° bins for source-receiver distances between 30° and 76°. (b) As in Figure 1a but for *ScP* between 30° and 65°. Note that the scale is logarithmic.

attenuation at the base of the mantle mimics a smaller reflection coefficient. Unfortunately, the depth dependence of mantle attenuation has not been determined precisely, so the correction for attenuation is the most uncertain of the amplitude factors. For *P* waves in the mantle we use *Warren and Shearer*'s [2000] two-layer compressional wave quality factor (Q_α) model, with the division between the upper and lower mantle at 660 km. We use the expression

$$Q_\beta = \frac{4}{9} Q_\alpha \tag{2}$$

to obtain attenuation for the *S* leg of *ScP* (Q_β is the shear wave quality factor).

[14] One limitation of *Warren and Shearer*'s [2000] model is its lack of resolution in the lower mantle, but an overriding advantage is that it was derived within the same frequency range we examine. *Warren and Shearer* [2000] present frequency-independent and frequency-dependent versions of their model. In general, mantle attenuation is most likely frequency dependent [e.g., *Anderson and Given*, 1982; *Choy and Cormier*, 1986]. For *PcP* the two versions of the model do not yield very different results. However, in tests of *ScP* amplitudes, the very high Q_β in the frequency-independent case does not sufficiently attenuate shear waves to match our data. Similarly, *Bock and Clements* [1982] found that frequency-dependent attenuation in the lower mantle was required to match their *ScP* data sampling the CMB between Tonga and Australia. Thus we employ the frequency-dependent version of *Warren and Shearer*'s [2000] model. Table 1 gives Q_α and Q_β as a function of frequency and depth.

Table 1. Q_α Model From *Warren and Shearer* [2000][a]

	Frequency, Hz		
Depth, km	1.0	0.55	0.3
	Q_α		
0–660	298.0	230.9	200.0
660–2891	1230.0	893.5	738.9
	Q_β		
0–660	132.4	102.6	88.9
660–2891	546.7	397.1	328.4

[a] $Q_\beta = (4/9)Q_\alpha$.

[15] After applying the amplitude corrections, we take the logarithms of the envelope functions and sum them. Since we cannot check each corrected trace individually, stacking logarithms guards against any anomalous seismograms dominating the stack. After stacking, we divide by the number of seismograms and compute the antilog.

[16] We repeat this processing for the *P* wave on every seismogram to compute a separate *P*-aligned stack corresponding to each core reflection-aligned stack. This is necessary because the source and path amplitude corrections are different for *P* than for *PcP* or *ScP*. It also avoids the broadening of *P* arrivals that would result in stacks aligned on the core reflections as a consequence of combining earthquakes from a range of source depths and distances.

3. Globally Averaged Reflection Properties

3.1. Stacks

[17] Stacks aligned on *PcP* and *ScP* are shown in Figures 2 and 3, respectively. The envelope of the *P*-generated coda is clearly a significant source of noise even 100 s after the *P* arrival. The coda results from the scattering of seismic waves near the source and receiver. This decaying noise envelope is especially problematic at greater epicentral distances, where *PcP* arrives closer in time to *P*. Crossing phases such as *PP* and *S* are more easily observed at low frequencies (Figure 3). These phases are highly attenuated at short periods because of the extra legs in the upper mantle in the case of *PP* and the greater intrinsic attenuation associated with shearing motions in the case of *S*. The coda is also more attenuated at high frequencies, making *PcP* and *ScP* easier to observe.

3.2. Amplitude Ratios

[18] To measure amplitude ratios (*PcP*/*P* or *ScP*/*P*), we must measure the amplitude of the core reflection above that of the decaying coda envelope on each stack. We estimate the coda envelope by fitting a linear function to it before the signal phase and extrapolating it into the signal window. In practice, this is a somewhat difficult procedure for the core reflections because contamination from crossing phases such as *pP*, *sP*, *PP*, and *S* sometimes disrupts the smooth decay. Accordingly, we adjust the time window in which we perform the fit to avoid these phases. The windows typically are <10 s long and are within 10 s of the core reflection, so the linear assumption holds.

[19] The signal amplitude (*PcP* or *ScP*) is the total envelope minus, in a root-mean-square sense, the extrapolated noise function. We measure the total envelope by finding the peak around the expected arrival time and then averaging the envelope in a 4-s window surrounding it. This provides a more stable value than simply taking the peak. We perform the same procedure on the *P* wave stacks. We then divide to obtain the amplitude ratio *PcP*/*P* or *ScP*/*P*.

[20] The amplitude ratios as a function of distance are plotted in Figures 4 and 5. The amplitude ratios generally agree with previous observations [e.g., *Müller et al.*, 1977; *Schlittenhardt*, 1986; *Castle and van der Hilst*, 2000]. Estimates of the background envelope are sensitive to the time windows chosen, so we consider oscillations of the ratios more likely to be indicative of the uncertainty of the measurement than of range-dependent variations.

[21] The high *PcP*/*P* amplitude ratios around 40° in the 0.25- to 0.5-Hz band pass (Figure 4) result from the coincident arrival of *PP* with *PcP* at that distance. *PP* is stronger at long periods; hence its effect is reduced in the other frequency ranges.

[22] Averages of the three band passes are also plotted in Figures 4 and 5 as broadband averages. This provides a better estimate of the broadband reflection properties than would be obtained from initially filtering with a wide band pass, which would be dominated by long periods. The broadband averages exclude 0.25- to 0.5-Hz data between 37° and 45° for *PcP* and between 35° and 40° for *ScP* so that the effects of crossing phases *PP* and *S*, respectively, do not contaminate the range dependence.

[23] The amplitude ratios measure the reflection coefficients at the CMB, which depend on the impedance contrast and incidence angle. By varying velocity and density parameters above the CMB, we compute the effects on reflection coefficients and compare them with the observations. We assume here plane waves incident on a flat boundary. The resulting reflection coefficients are independent of frequency [*Aki and Richards*, 1980]. These conditions are realistic because the CMB is locally flat with no apparent major topography [e.g., *Earle and Shearer*, 1997] and curvature is unimportant. We compare the broadband-averaged amplitude ratios against predictions of *PcP* and *ScP* reflection coefficients from the preliminary reference Earth model (PREM) [*Dziewonski and Anderson*, 1981] and several representative ULVZ models with velocity reductions and density increases relative to PREM (Figures 6 and 7).

[24] Velocity reductions and density increases in the mantle would bring its values closer to those of the core, so the reflected amplitudes would be reduced. The range dependence changes slightly as well, which is most evident for *ScP* at greater distances. In PREM the reflection coefficient rises sharply near the critical distance because of the increasingly vertical polarization of the downgoing *S* leg. In the ULVZ models this effect is sharply reduced. We are ignoring potential scattering of the incident wave because of reflections at the upper boundary of a ULVZ or heterogeneity within it. Since both effects would reduce the predicted amplitudes of *PcP* or *ScP*, our measured amplitude ratios may represent slight underestimates of the reflection coefficients. That is, observed amplitudes lower than the model predictions could result from a combination of reduced reflection coefficient and losses due to attenuation and scattering.

[25] The *PcP*/*P* broadband average does not match ULVZs with V_P and V_S reductions of 10 and 30%,

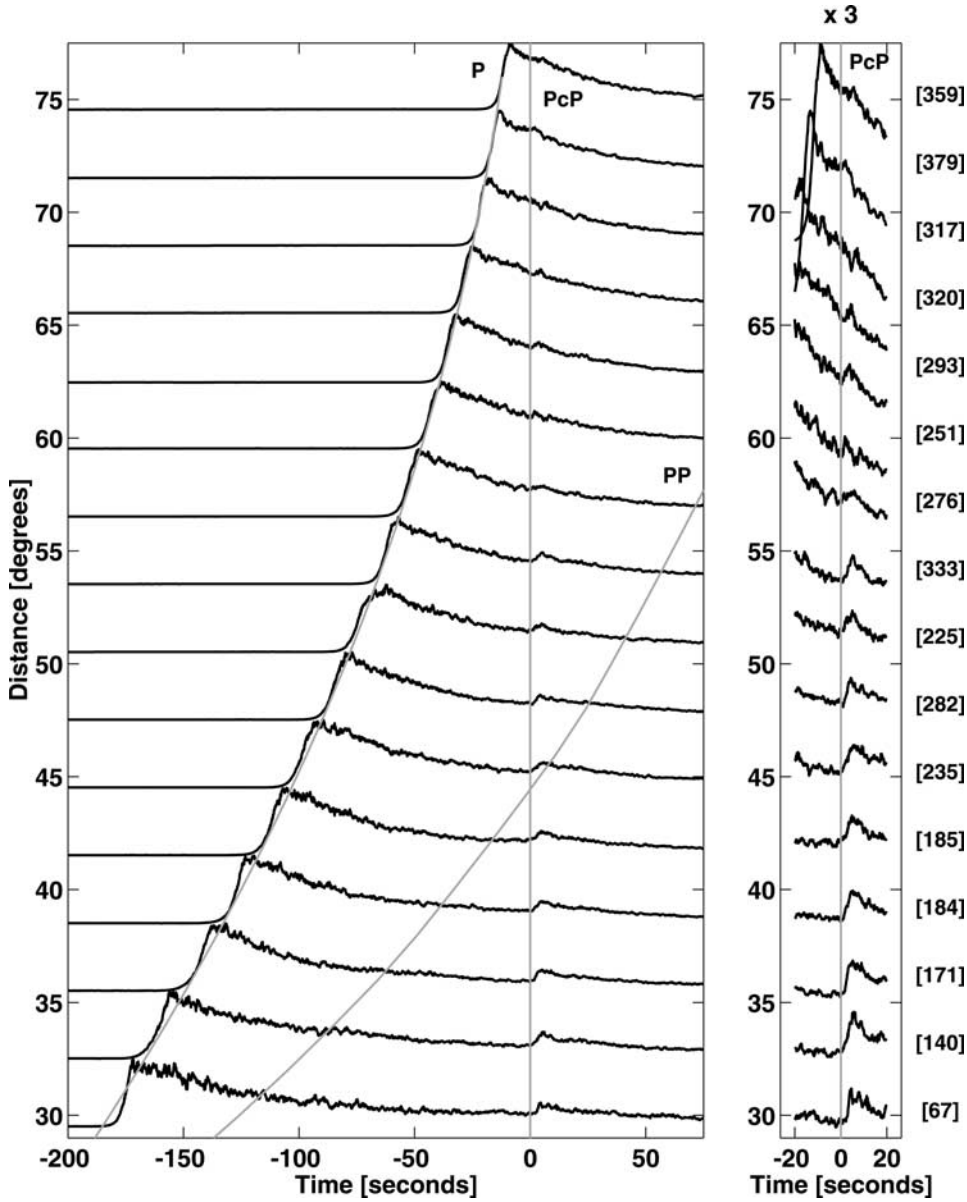

Figure 2. Stacks aligned on *PcP* in 3° distance bins, band-pass filtered between 1.0 and 2.0 Hz. The expected arrival times of *P*, *PcP*, and *PP* are shown by lightly shaded lines. The right panel shows the window from 20 s before *PcP* to 20 s after, magnified by a factor of 3. The number of seismograms in each stack is given on the right axis. At close distances, *PcP* is easily observed. At distances beyond ~55°, *PcP* becomes less visible above the background as the *P*-generated coda dominates the envelope.

respectively (Figure 6). For *PcP*/*P* between about 30° and 50°, where it is easiest to measure because of lower coda, the ULVZ model with 10% reductions in both V_P and V_S and a density increase of 20% is slightly preferred over PREM and a ULVZ model with 10% V_P and V_S reductions and no density change, although the latter two models cannot be rejected. Beyond ~50° the increased coda noise makes *PcP* amplitudes more difficult to measure. The difficulty of fitting the noise window at larger distances is increased because *PcP* is closer in time to *P*, and depth phases *pP* and *sP* arrive between them. The largest predicted difference between these ULVZs and PREM is expected at greater distances, but the high variability of the amplitude ratios at large epicentral range prevents derivation of strong constraints from those measurements.

[26] We also considered a core-mantle transition zone (CMTZ) model in which the velocities and density gradationally change from mantle to core values. To estimate the effect on reflection amplitudes, we computed the pulse broadening due to the travel time delays through the layer and compared the amplitudes of the broadened pulses at long and short periods. At longer periods we expect the thin transition zone to be essentially invisible to the waves, but at shorter periods such as 1 s the reflected phase should be sensitive to the CMTZ. For a CMTZ of thickness 3 km we

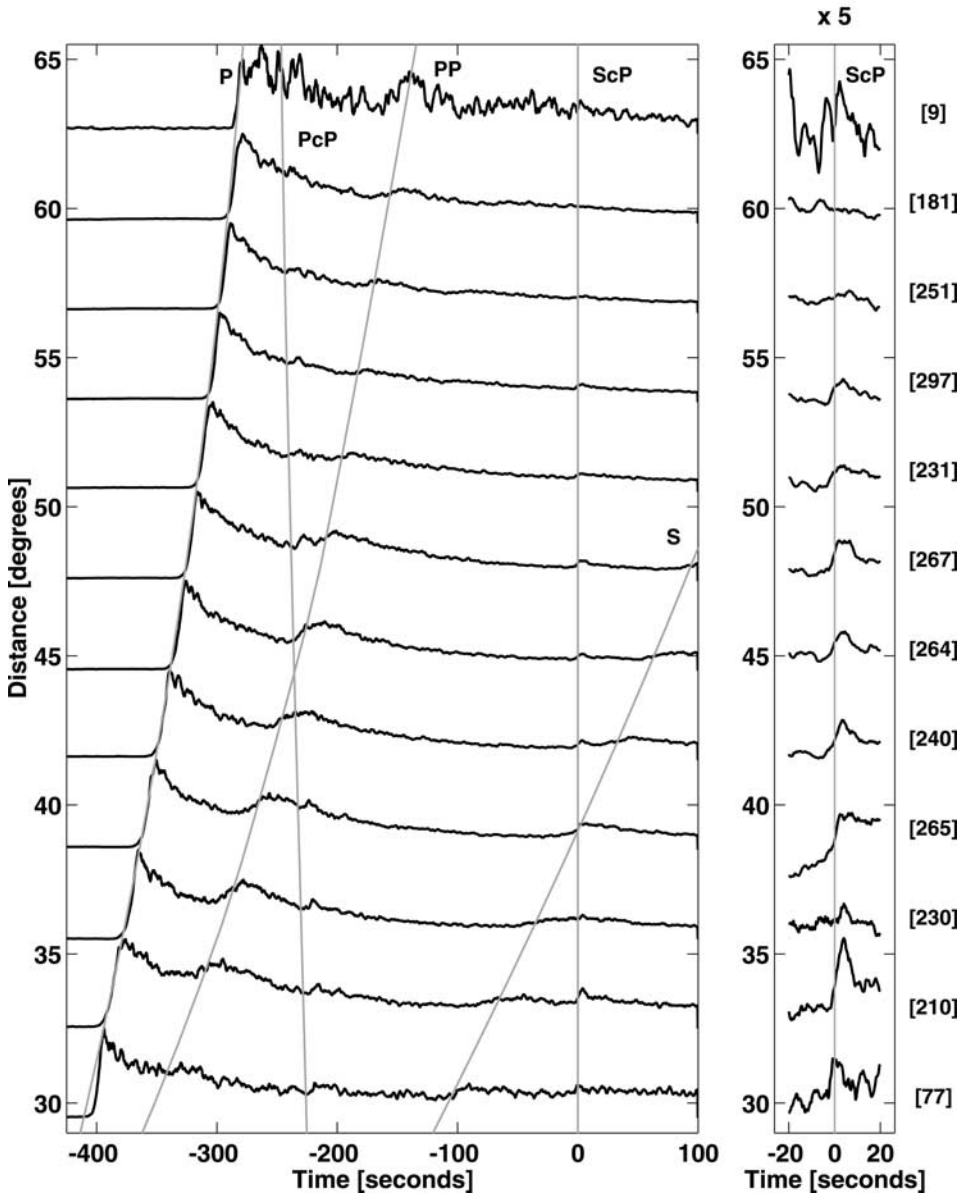

Figure 3. Stacks aligned on *ScP* in 3° distance bins, band-pass filtered between 0.25 and 0.5 Hz. The expected arrival times of *P*, *PcP*, *PP*, *ScP*, and *S* are shown by lightly shaded lines. The right panel shows the window from 20 s before *ScP* to 20 s after, magnified by a factor of 5. The number of seismograms in each stack is given on the right axis. Both *PP* and *S* are visible as broad peaks along their travel time curves.

find that the 1-Hz amplitude would be reduced to less than half the 0.3-Hz amplitude. This reduction is not seen in the amplitude ratios (Figure 4). However, for a CMTZ thickness of 1 km, the high-frequency reflection would be ~90% that of the long period, a reduction that is not resolvable with our data.

[27] The *ScP*/*P* broadband average generally agrees with PREM in both amplitude and range dependence (Figure 7). However, the 0.25- to 0.5-Hz band pass matches the predictions of PREM most closely, while the shorter-period band passes yield higher amplitudes than any model predicts. This is likely a result of underestimating Q_β in the model for shear waves at higher frequencies. Nevertheless, the range dependence of the higher-frequency band passes also matches that of PREM, suggesting that the ULVZ models are incompatible with these observations. The CMTZ models predict that a 3-km-wide zone should reduce 1-Hz amplitudes by >75%, which is not evident in the measurements.

[28] The average CMB for the regions we sample does not appear to have a highly attenuating basal layer with large shear wave velocity reductions. Comparing the coverage of the CMB (Figure 1) with the observations of ULVZs [*Williams et al.*, 1998], our densest coverage spans regions both with ULVZs (Mexico and Central America) and without them (southern and eastern Asia).

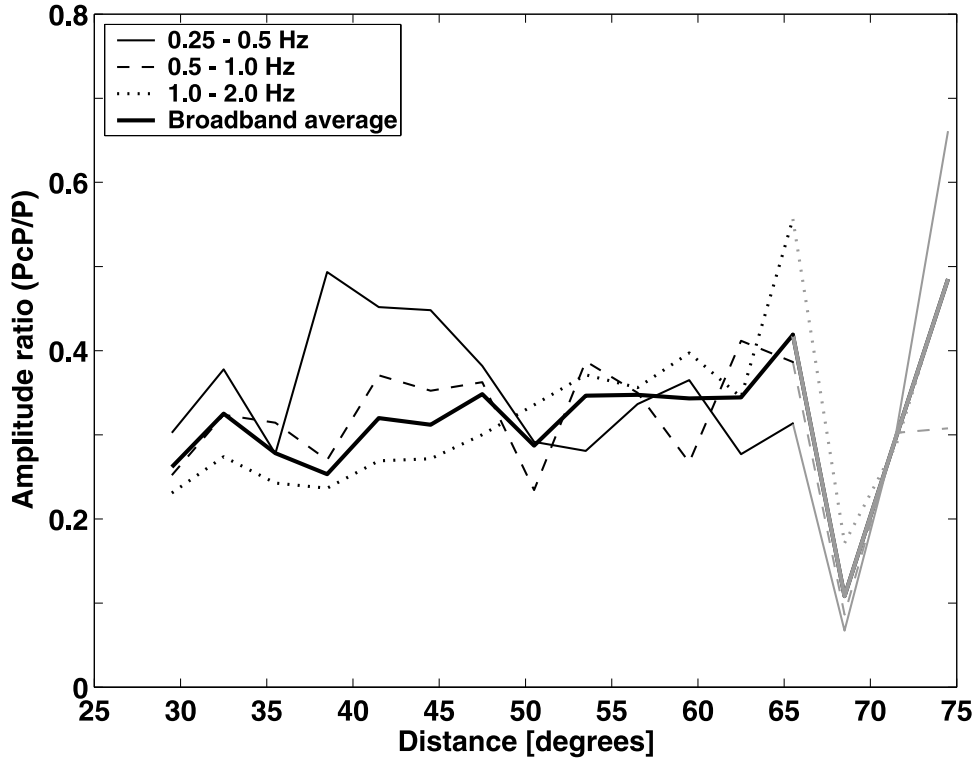

Figure 4. *PcP*/*P* versus distance in three band passes (0.25–0.5 Hz, 0.5–1.0 Hz, and 1.0–2.0 Hz). The thick solid line represents a broadband averaging of the three band-pass curves (excluding 0.25- to 0.5-Hz data between 37° and 45°, where *PP* arrives coincident with *PcP*) is shown. Data beyond 65.5° are lightly shaded because high coda levels between *P* and *PcP* make the amplitude ratios less reliable.

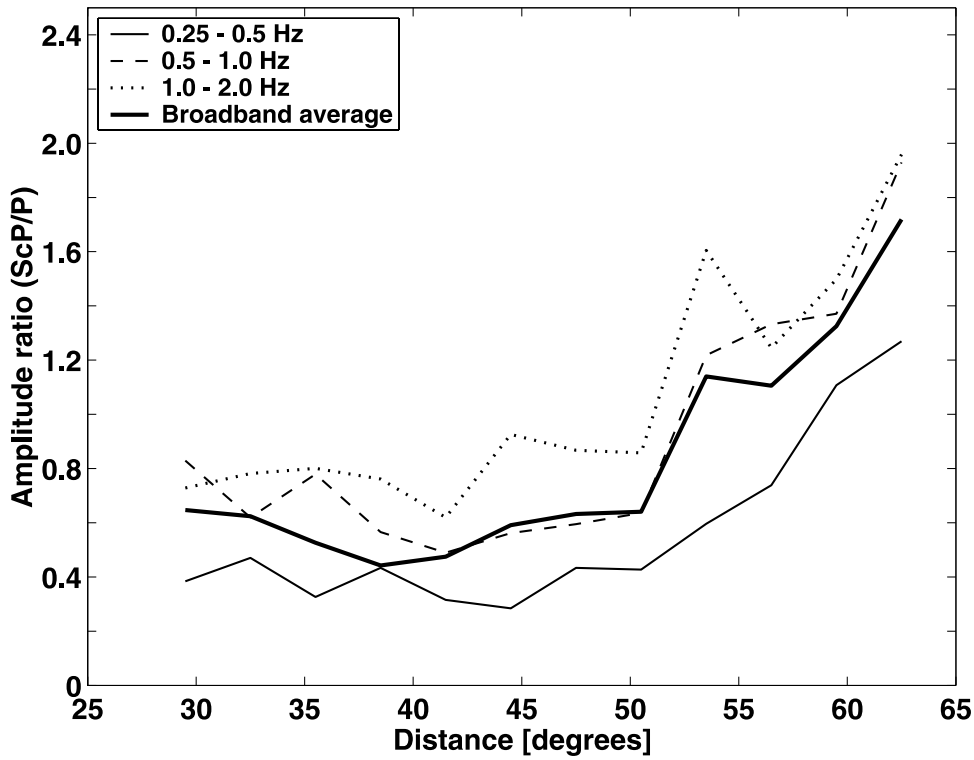

Figure 5. *ScP*/*P* versus distance in three band passes (0.25–0.5 Hz, 0.5–1.0 Hz, and 1.0–2.0 Hz). The thick solid line represents a broadband averaging of the three band-pass curves (excluding 0.25- to 0.5-Hz data between 35° and 40°, where *S* arrives coincident with *ScP*).

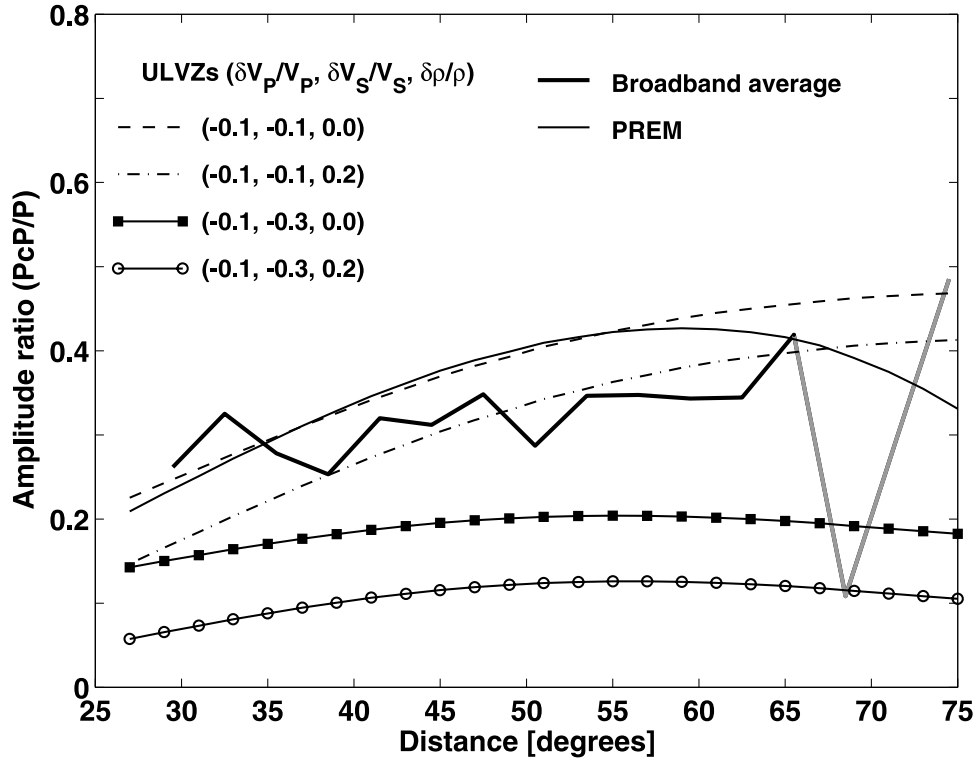

Figure 6. Comparison of broadband average *PcP*/*P* with PREM and four ULVZ models (with fractional changes in velocity and density indicated). The data do not match ULVZs with 30% V_S reduction. Between about 30° and 50°, where lower coda makes *PcP*/*P* measurements more reliable, the ULVZ model with 10% reductions in both V_P and V_S and a density increase of 20% is slightly preferred over PREM and a ULVZ with 10% V_P and V_S reductions and no density change, although the latter two models cannot be rejected. Beyond 65.5° the data curve is lightly shaded because the measurements have greater uncertainty.

However, the region with strongest evidence for ULVZs (southwest Pacific) is not well sampled by the core reflections.

4. Lateral Variations of Reflection Properties

[29] With evidence for lateral variability of CMB region properties such as the D″ discontinuity, ULVZ existence and velocity reduction, and anisotropy, it is possible to postulate lateral variations in CMB reflection properties as well. Our stacking process is the same as for the global stacks, with the following exceptions: We apply a grid to the CMB surface (15° × 15°) and compute the location of each *PcP* or *ScP* bounce point. Rather than bin by source-receiver distance, we compute a stack for each grid element from seismograms with bounce points within it. To account for variation of the reflection coefficient with incidence angle, we use the predicted range dependence curve for PREM to adjust every seismogram to a source-receiver distance of 55°. Finally, for the 0.25- to 0.5-Hz and 0.5- to 1.0-Hz band passes, we exclude seismograms in the distance ranges from 39° to 45° (*PcP*) and from 37° to 39° (*ScP*) to avoid contamination from crossing phases *PP* and *S*.

[30] The bin size of 15° × 15° represents a compromise between the desire to map on as fine a scale as possible and the need to have sufficient numbers of seismograms in each stack to have adequate signal-to-noise ratio. Even with elements this size, many bins have only a few hits, and the coverage is uneven (Figure 1). We measure the *PcP*/*P* and *ScP*/*P* ratios in the same manner as on the globally averaged stacks and map them to the bounce point locations for those bins with at least eight seismograms stacked (Figures 8 and 9).

[31] Subdividing the data to this extent decreases the signal-to-noise ratio of the stacks. Most bins have fewer than 100 hits; this contrasts with the global averages binned by distance, where each stack contained hundreds of seismograms. As a result, the random fluctuations in the stacks are not averaged out as effectively, and amplitude ratios can be very sensitive to the placement of windows. The effects can be seen in Figures 8 and 9: The most anomalous bins tend to have around 20 or fewer hits. Those with more than 100 are more stable and have smaller deviations from PREM.

[32] We consider several regions where coverage is greatest. Under Mexico and the Caribbean Sea, *PcP* trends from PREM-like amplitudes to lower values from west to east. *ScP* has a similar pattern. *Persh et al.* [2001] previously found no evidence for ULVZ precursors in that region, which is consistent with a PREM-like CMB. The east-west trend agrees with patterns observed by *Havens and Revenaugh* [2001].

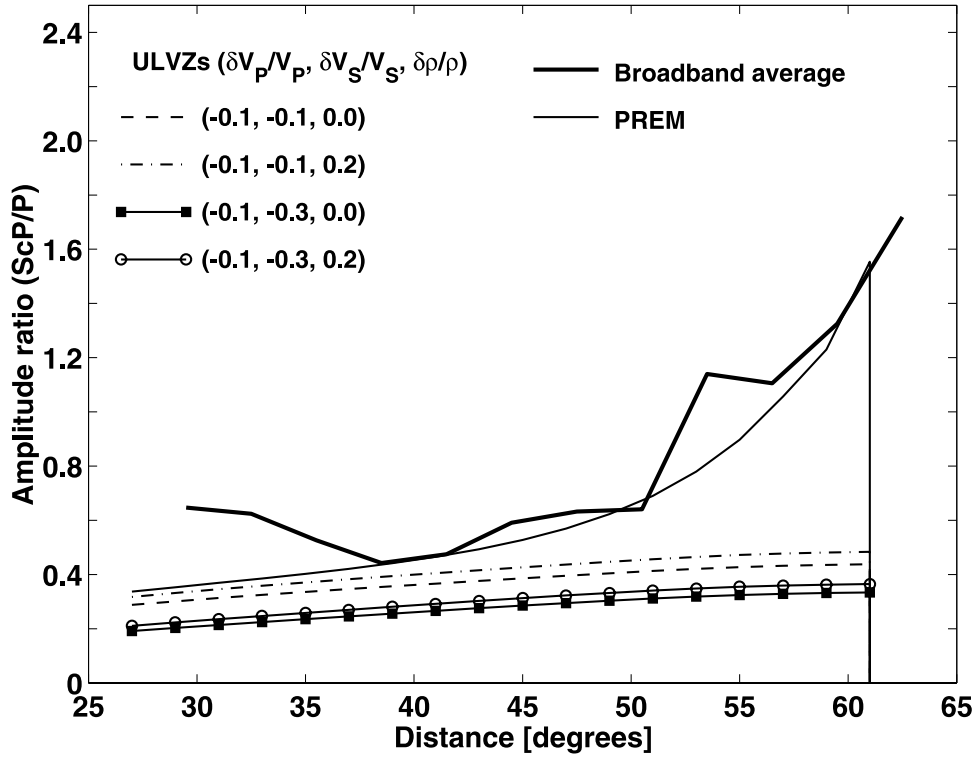

Figure 7. Comparison of broadband average *ScP*/*P* with PREM and four ULVZ models (with fractional changes in velocity and density indicated). The amplitude and trend with distance most closely match the predictions from PREM.

[33] In the northeast Pacific, another region where *Persh et al.* [2001] did not find ULVZ precursors, *PcP* has normal to somewhat high amplitudes, while *ScP* has somewhat low amplitudes. *Castle and van der Hilst* [2000] found strong *ScP* in that region. Under the western Pacific and eastern Asia, *PcP* has low to PREM-like amplitudes trending to somewhat higher values toward the northwest, while *ScP* does not display a consistent pattern. The small numbers of

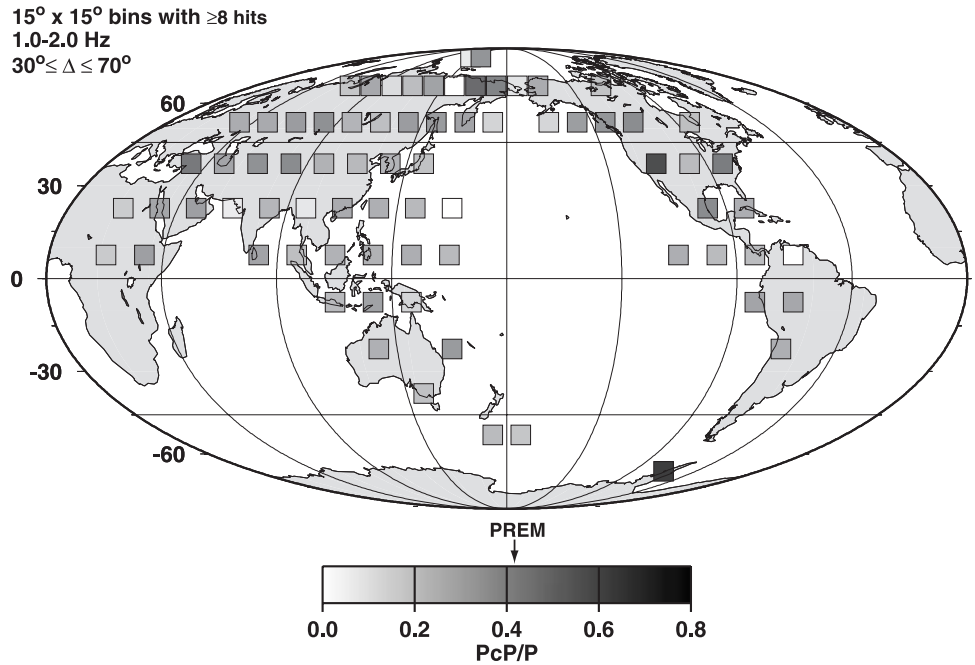

Figure 8. *PcP*/*P* from stacks in 15° × 15° bins at the CMB. Band pass is 1.0–2.0 Hz. Seismograms from distances 30°–70° are used and corrected for incidence angle to 55°. Only bins with at least eight stacked seismograms are plotted. Value for PREM at 55° is indicated on scale.

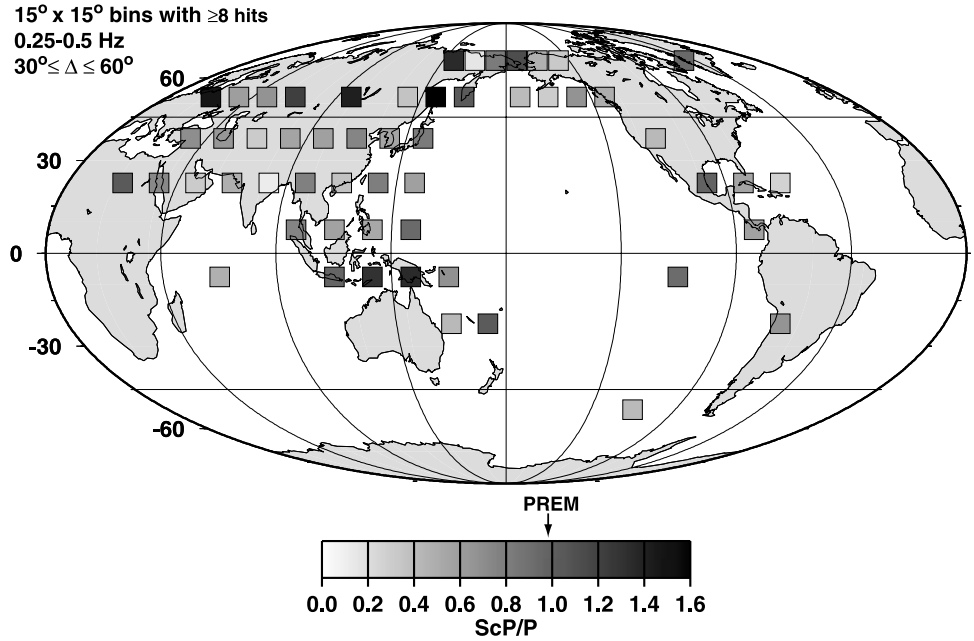

Figure 9. *ScP*/*P* from stacks in 15° × 15° bins at the CMB. Band pass is 0.25–0.5 Hz. Seismograms from distances 30°–60° are used (excluding those between 37° and 39°, where *S*-generated noise is greatest) and corrected for incidence angle to 55°. Only bins with at least eight stacked seismograms are plotted. Value for PREM at 55° is indicated on scale.

seismograms contribute to the variability, which along with incomplete coverage, precludes firm conclusions at this point.

5. Discussion

[34] Our measurements from globally averaged stacks of *PcP* and *ScP* are consistent with PREM but also allow weak low-velocity layers above the CMB. The amplitude ratios rule out worldwide average *S* wave velocity reductions of 30% as well as a 3-km-wide core-mantle transition zone. This observation is consistent with previous results indicating a CMB thickness less than ~1 km [*Kanamori*, 1967; *Vidale and Benz*, 1992]. Given the scatter of our measurement, with *PcP*/*P* we cannot distinguish between PREM and a model with 10% reductions in both V_P and V_S and up to a 20% increase in density. The *ScP*/*P* amplitudes are more consistent with PREM, but corrections for mantle attenuation of *S* waves at high frequencies are uncertain. These observations argue against a globally constant layer overlying the CMB, consistent with recent observations of strong lateral variations of ULVZ properties [*Rost and Revenaugh*, 2003].

[35] Although localized regions with extreme velocity reductions exist [e.g., *Vidale and Hedlin*, 1998; *Wen and Helmberger*, 1998], this study suggests they are not present globally. Thus explanations for ULVZs such as pressure-dependent phase changes in mantle constituents are less likely since they would lead to more globally consistent features. The lateral variations and the most extreme ULVZ observations therefore likely require the local presence of compositional anomalies. This provides further support for interpretations of V_S/V_P ratios and density variations in tomography models of the lower mantle [e.g., *Van der Hilst et al.*, 1998; *Ishii and Tromp*, 1999]. Dynamical processes such as subduction or thermal instabilities could drive the formation and organization of such compositional heterogeneities.

[36] Mapping reflection amplitudes to the CMB bounce points reveals lateral variations in CMB reflection properties. The limited number of regions with dense coverage is an impediment, but in the best sampled regions we detect patterns that are consistent with previous detections and nondetections of ULVZs.

[37] Future supplements to the coverage of the data set employed here can include data from temporary seismic instrument deployments and other seismic phases, such as the underside reflection *PKKP*. CMB reflectivity could then be compared with patterns of tomography and ULVZ observations. The question of fine structure overlying the CMB will benefit from further studies using seismic phases with localized sampling.

[38] **Acknowledgments.** We thank Associate Editor Ed Garnero and referees Sebastian Rost and Vernon Cormier for careful reviews that improved this paper, including the suggestion to add the discussion of lateral variations. This work was supported by NSF grants EAR9902995 and EAR0001126. Figures 1, 8, and 9 were created using GMT version 3.0 [*Wessel and Smith*, 1995].

References

Aki, K., and P. Richards (1980), *Quantitative Seismology, Theory and Methods*, W. H. Freeman, New York.

Anderson, D. L., and J. W. Given (1982), Absorption band *Q* model for the Earth, *J. Geophys. Res.*, *87*, 3893–3904.

Bock, G., and J. R. Clements (1982), Attenuation of short-period *P*, *PcP*, *ScP*, and *pP* waves in the Earth's mantle, *J. Geophys. Res.*, *87*, 3905–3918.

Buffett, B. A., E. J. Garnero, and R. Jeanloz (2000), Sediments at the top of Earth's core, *Science*, *290*, 1338–1342.

Castle, J. C., and R. D. van der Hilst (2000), The core-mantle boundary under the Gulf of Alaska: No ULVZ for shear waves, *Earth Planet. Sci. Lett.*, *176*, 311–321.

Choy, G. L., and V. F. Cormier (1986), Direct measurement of the mantle attenuation operator from broadband *P* and *S* waveforms, *J. Geophys. Res.*, *91*, 7326–7342.

Dziewonski, A. M., and D. L. Anderson (1981), Preliminary reference Earth model, *Phys. Earth Planet. Inter.*, *25*, 297–356.

Earle, P. S., and P. M. Shearer (1997), Observations of *PKKP* precursors used to estimate small-scale topography on the core-mantle boundary, *Science*, *277*, 667–670.

Earle, P. S., and P. M. Shearer (2001), Distribution of fine-scale mantle heterogeneity from observations of P_{diff} coda, *Bull. Seismol. Soc. Am.*, *91*, 1875–1881.

Garnero, E. J., and D. V. Helmberger (1996), Seismic detection of a thin laterally varying boundary layer at the base of the mantle beneath the central-Pacific, *Geophys. Res. Lett.*, *23*, 977–980.

Garnero, E. J., and D. V. Helmberger (1998), Further structural constraints and uncertainties of a thin laterally varying ultralow-velocity layer at the base of the mantle, *J. Geophys. Res.*, *103*, 12,495–12,509.

Garnero, E. J., and R. Jeanloz (2000), Fuzzy patches on the Earth's core-mantle boundary?, *Geophys. Res. Lett.*, *27*, 2777–2780.

Garnero, E. J., and J. E. Vidale (1999), ScP; a probe of ultralow velocity zones at the base of the mantle, *Geophys. Res. Lett.*, *26*, 377–380.

Garnero, E. J., J. Revenaugh, Q. Williams, T. Lay, and L. H. Kellogg (1998), Ultralow velocity zone at the core-mantle boundary, in *The Core-Mantle Boundary Region*, *Geophys. Monogr. Ser.*, vol. 28, edited by M. Gurnis et al., pp. 319–334, AGU, Washington, D. C.

Havens, E., and J. Revenaugh (2001), A broadband seismic study of the lowermost mantle beneath Mexico: Constraints on ultralow velocity zone elasticity and density, *J. Geophys. Res*, *106*, 30,809–30,820.

Helmberger, D., S. Ni, L. Wen, and J. Ritsema (2000), Seismic evidence for ultralow-velocity zones beneath Africa and eastern Atlantic, *J. Geophys. Res.*, *105*, 23,865–23,878.

Holland, K. G., and T. J. Ahrens (1997), Melting of $(Mg,Fe)_2$ SiO_4 at the core-mantle boundary of the Earth, *Science*, *275*, 1623–1625.

Ishii, M., and J. Tromp (1999), Normal-mode and free-air gravity constraints on lateral variations in velocity and density of Earth's mantle, *Science*, *285*, 1231–1236.

Kanamori, H. (1967), Spectrum of *P* and *PcP* in relation to the mantle-core boundary and attenuation in the mantle, *J. Geophys. Res.*, *72*, 559–571.

Kennett, B. L. N., and E. R. Engdahl (1991), Travel times for global earthquake location and phase association, *Geophys. J. Int.*, *105*, 429–465.

Knittle, E. (1998), The solid/liquid partitioning of major and radiogenic elements at lower mantle pressures: Implications for the core-mantle boundary region, in *The Core-Mantle Boundary Region*, *Geophys. Monogr. Ser.*, vol. 28, edited by M. Gurnis et al., pp. 119–130, AGU, Washington, D. C.

Lay, T., and T. C. Wallace (1995), *Modern Global Seismology*, Academic, San Diego, Calif.

Manga, M., and R. Jeanloz (1996), Implications of a metal-bearing chemical boundary layer in D″ for mantle dynamics, *Geophys. Res. Lett.*, *23*, 3091–3094.

Mori, J., and D. V. Helmberger (1995), Localized boundary layer below the mid-Pacific velocity anomaly identified from a *PcP* precursor, *J. Geophys. Res.*, *100*, 20,359–20,365.

Müller, G., A. H. Mula, and S. Gregersen (1977), Amplitudes of long-period *PcP* and the core-mantle boundary, *Phys. Earth Planet. Inter.*, *14*, 30–40.

Persh, S. E., J. E. Vidale, and P. S. Earle (2001), Absence of short-period ULVZ precursors to *PcP* and *ScP* from two regions of the CMB, *Geophys. Res. Lett.*, *28*, 387–390.

Reasoner, C., and J. Revenaugh (1999), Short period *P* wave constraints on D″ reflectivity, *J. Geophys. Res.*, *104*, 955–961.

Revenaugh, J., and R. Meyer (1997), Seismic evidence of partial melt within a possibly ubiquitous low-velocity layer at the base of the mantle, *Science*, *277*, 670–673.

Rost, S., and J. Revenaugh (2003), Small-scale ultralow-velocity zone structure imaged by *ScP*, *J. Geophys. Res.*, *108*(B1), 2056, doi:10.1029/2001JB001627.

Schlittenhardt, J. (1986), Investigation of the velocity- and Q-structure of the lowermost mantle using *PcP*/*P* amplitude ratios from arrays at distances of 70°–84°, *J. Geophys.*, *60*, 1–18.

Sidorin, I., M. Gurnis, and D. V. Helmberger (1999), Evidence for a ubiquitous seismic discontinuity at the base of the mantle, *Science*, *286*, 1326–1331.

Tackley, P. J. (1998), Three-dimensional simulations of mantle convection with a thermo-chemical basal boundary layer: D″?, in *The Core-Mantle Boundary Region*, *Geophys. Monogr. Ser.*, vol. 28, edited by M. Gurnis et al., pp. 231–253, AGU, Washington, D. C.

Van der Hilst, R. D., S. Widiyantoro, K. C. Creager, and T. J. McSweeney (1998), Deep subduction and aspherical variations in *P* wavespeed at the base of the mantle, in *The Core-Mantle Boundary Region*, *Geophys. Monogr. Ser.*, vol. 28, edited by M. Gurnis et al., pp. 5–20, AGU, Washington, D. C.

Vidale, J. E., and H. M. Benz (1992), A sharp and flat section of the core-mantle boundary, *Nature*, *359*, 627–629.

Vidale, J. E., and M. A. H. Hedlin (1998), Evidence for partial melt at the core-mantle boundary north of Tonga from the strong scattering of seismic waves, *Nature*, *391*, 682–685.

Warren, L. M., and P. M. Shearer (2000), Investigating the frequency dependence of mantle Q by stacking *P* and *PP* spectra, *J. Geophys. Res.*, *105*, 25,391–25,402.

Wen, L. (2000), Intense seismic scattering near the Earth's core-mantle boundary beneath the Comoros hotspot, *Geophys. Res. Lett.*, *27*, 3627–3630.

Wen, L., and D. V. Helmberger (1998), Ultra-low velocity zones near the core-mantle boundary from broadband *PKP* precursors, *Science*, *279*, 1701–1703.

Wessel, P., and W. H. F. Smith (1995), New version of the Generic Mapping Tools released, *Eos Trans. AGU*, *76*, 329.

Williams, Q., and E. J. Garnero (1996), Seismic evidence for partial melt at the base of Earth's mantle, *Science*, *273*, 1528–1530.

Williams, Q., J. Revenaugh, and E. J. Garnero (1998), A correlation between ultra-low basal velocities in the mantle and hot spots, *Science*, *281*, 546–549.

S. E. Persh and J. E. Vidale, Department of Earth and Space Sciences, University of California, Los Angeles, CA 90095-1567, USA. (spersh@moho.ess.ucla.edu; vidale@ucla.edu)